Passive Intermodulation Distortion in Antennas

Jonathan R. Wilkerson, *Member, IEEE*, Ian M. Kilgore, *Student Member, IEEE*, Kevin G. Gard, *Member, IEEE*, and Michael B. Steer, *Fellow, IEEE*

Abstract—An analytic formulation of passive intermodulation distortion (PIM) in antennas is presented for PIM introduced by electro-thermal modulation of conductivity by current-related losses. A silver rectangular patch antenna was fabricated using a sapphire substrate isolating the thermal process from other possible sources. Two-tone testing at 990 MHz using a sweep of the tone separation from 3 Hz to 100 kHz is reported. Both transmitted and reflected PIM are characterized using a high dynamic range two-tone test system incorporating an analog canceler achieving a dynamic range of 125 dB at 1-Hz tone separation for reflection measurements, and 100 dB at 10-Hz tone separation for transmission measurements with each tone set to 32.3 dBm.

Index Terms—Antenna distortion, intermodulation distortion, microstrip patch antenna, nonlinear distortion, passive intermodulation distortion (PIM), two-tone test.

I. INTRODUCTION

PASSIVE intermodulation distortion (PIM) in circuits, transmission lines, and antennas establishes fundamental limits of performance for wireless sensor, communication, radar, and navigation systems. The present work was motivated by the need to understand the interference in a sensitive receiver when located adjacent to a high power transmitter, so-called co-site interference. In the classic two-tone test of PIM, two radio frequency (RF) tones, one at frequency f_1 and the other at f_2 are applied to a structure such as an antenna. If there is PIM, then the resulting spectrum is as shown in Fig. 1. The additional tones at f_3 and f_4 result from distortion and are called the upper and lower PIM, respectively, if the structure being tested is electrically passive. Many physical mechanisms including ferromagnetic effects, thermionic emission, field emission, tunneling, and micro-discharge have been suggested as physical mechanisms generating PIM on antenna structures [1]–[6].

Tunneling in reflector antennas has been studied as a source of PIM where the use of aluminum (Al) panels creates $Al - Al_2O_3 - Al$ (metal-oxide) junctions of the correct dimension, 2–3 nm, to produce tunneling [7], [8] and thus PIM. PIM has been observed by the authors with an assembled Yagi-Uda antenna with screw-attached Al elements and the PIM greatly reduced when the elements were Al-welded. In general, antennas
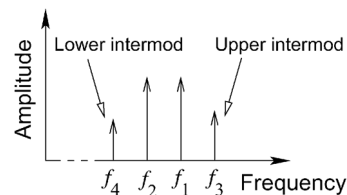
Fig. 1. Spectrum with two tones applied to a structure producing upper and lower PIM (i.e., intermodulation tones or intermods) at frequencies f_3 and f_4.

such as dipoles which do not possess junctions that would support tunneling still produce PIM [9].

In [10], high current densities and magnetic materials were shown to increase PIM in antenna structures, although no physical mechanism for the PIM dependency on current density was suggested. It is not always feasible to eliminate magnetic materials as chrome (an antiferromagnetic and paramagnetic material) and nickel (a ferromagnetic material) are commonly used as seed layers having excellent adhesion properties. Still a particular antenna can be designed to minimize the impact of magnetic materials and there are alternate antenna designs that do not require magnetic materials. In antennas that do not have metal-oxide junctions, PIM mechanisms are generally lumped together and explained through heuristic models rather than physically based models. Many theoretical studies have been undertaken as to the sources of PIM, but there has been limited experimental evidence coupled with theoretical analysis that has isolated PIM effects in modern RF and microwave systems. Magnetic and tunneling effects can be eliminated through material and fabrication choice. Thermionic and field emission as well as micro-discharge cannot be eliminated as sources of PIM, but their effects can be suppressed by operating under medium power density conditions and minimizing surface roughness. These are voltage-, i.e., electric field-, dependent effects rather than the current density dependence suggested in [10]. With ferromagnetic and junction effects eliminated, the remaining source of PIM is an electrothermal effect [11], [12].

In this paper, electro-thermal conductivity modulation is presented as a physical mechanism for PIM generation on antennas and resonant structures in general. In Section III, the PIM generated by an antenna due to heating from a standing wave current is developed. The design of a single metal silver-on-sapphire rectangular patch antenna is described in Section IV, and Section V describes the fabrication techniques used to minimize supposed sources of PIM other than the electro-thermal effect. Section VI describes the test system used to perform reflection and transmission PIM measurements and the extent taken to maximize dynamic range of the test system and minimize PIM in the measurement system itself. Section VI compares antenna PIM modeled as an electro-thermal effect to measurements indicating good agreement.

II. SYNOPSIS

The following development is involved, and so it is instructive to provide a synopsis. Heating is due to instantaneous power dissipation which is the product of instantaneous voltage and current. Heating then changes temperature and thus conductor resistance which results in RF signal distortion. With an RF signal, variations due to instantaneous heating are at the RF signal time scales, but this is only apparent in regions with submicron dimensions. This is based on a number of studies undertaken by us [13]–[16]. At distances of more than a micron, heating, temperature, and resistance variations only appear to respond to the amplitude of the RF signal. Thus for a low-to-moderate bandwidth RF signal, the effective heating tracks the envelope of the RF signal. For heating in a conductor on a substrate, heat can redistribute inside the metallic conductor and can also pass into the substrate. If the RF envelope variation is slow, heat distribution within the metal will uniformly heat the metal, and then the only heat flux path will be into the substrate. This is a consequence of the thermal conductivity of the metal being much higher than that of the substrate. For rapidly varying RF envelopes, heating within the metal will not be uniform, and heat flux will flow from a hot region into a cooler metallic region with the cooler metallic regions acting as a heatsink (or thermal capacitor).

Thus electro-thermal passive intermodulation is dependent on tone separation for a two-tone RF signal with a lowpass filter-like response with respect to tone separation (i.e., the rate at which the RF envelope varies). The lowpass corner frequency largely corresponds to transition from heat flow due to metallic heatsinking to heat flow into the substrate.

III. ELECTRO-THERMAL THEORY OF PIM ON ANTENNAS

Electro-thermal PIM generally has not been considered as a dominant PIM mechanism in antennas due to the predominately metal structure of antennas as well as the difference between thermal time constants and the period of high-frequency electrical signals. Previously electro-thermally induced PIM on a transmission line was shown to be due to thermal conductivity modulation within the electrical skin depth [12]. Similarly, currents on antennas are confined to a few skin depths and experience the same thermal conductivity modulation. Thermal conductivity modulation is enhanced in resonant structures such as resonant antennas due to a standing current wave resulting in enhanced resistive losses. The additional metallization and standing wave of a resonant antenna significantly alters the heat conduction environment from that of a transmission line. The heat conduction environment for a microstrip rectangular patch antenna is analyzed in Section III-A, yielding the temperature distribution in the conductive layer of the metal due to thermal conduction to low current regions on the antenna. Using the thermal solution developed, the electro-thermal PIM from an infinitesimal volume element of the metal is derived.

The rectangular patch antenna considered here is shown in Fig. 2 and is partitioned into a patch section and a feed line section. The feed line and the patch will both produce PIM. The feed line has an RF traveling wave and the production of PIM on the feed line was previously treated [12], and those results are not repeated here. The analysis below is for PIM production on the patch which has an RF standing wave at its frequency of operation. The form of the PIM equations are similar to that
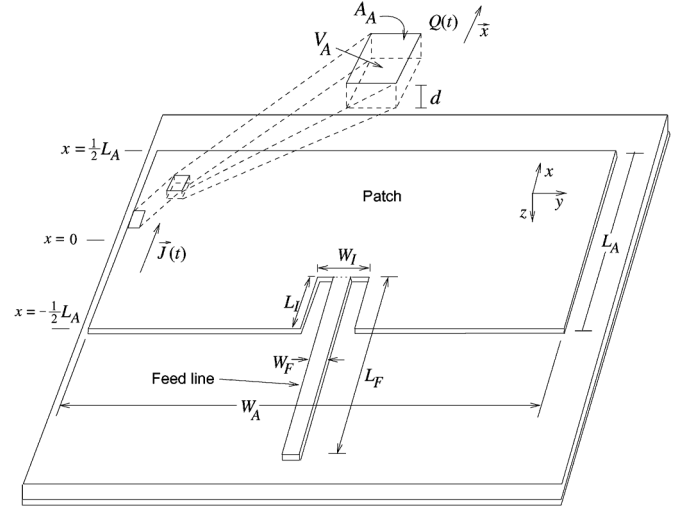

Fig. 2. Microstrip inset fed rectangular patch antenna with antenna width $W_A = 60$ mm and length $L_A = 45$ mm; inset width $W_I = 5.5$ mm and length $L_I = 9.0$ mm; and feed line of width $W_F = 411$ μm and length $L_F = 27.5$ mm. The sapphire substrate is $t_S = 500$ μm thick, and the silver metal is $t_A = 1.8$ μm thick. Infinitesimal loss elements have volume V, area A in the y-z plane, and thickness t_A.

developed for transmission lines in [12]. The main difference is in the definitions for the heat generating volume and the area through which heat flux passes.

A. Heat Conduction on a Rectangular Patch Antenna

Heat dissipation occurs in conductors due to finite conductivity. As the frequency of operation increases, the skin effect increases the current density, conductive loss, and thus heat generated. At RF, the resulting temperature variation is significant enough to alter the resistivity of conductors over time varying in unison with the envelope of the RF signal. Thus for a two-tone RF signal with the tones close in frequency, both the envelope and conductivity vary sinusoidally with a small localized variation of temperature, and hence conductivity, at the RF frequency. Variations of resistivity due to thermal modulation are known to produce PIM in microwave terminations, attenuators, integrated circuits, and transmission lines [11], [12], [17]. The PIM generated by an antenna through the electro-thermal process is derived below.

The patch can be thermally modeled as a semi-infinite heat conduction system. The metal of the antenna is bounded by air on all sides except at the interface with the dielectric. The thermal conductivity of air is at least two orders of magnitude below that of most electrical substrates and several orders of magnitude below that of metals, and so here, heat transfer in air is ignored. The resistive loss of the conductor is distributed across the structure intrinsically and thus is naturally partitioned into infinitesimal elements where the depth, d, of the heating cell is given by approximately twice the electrical skin depth, δ (one skin depth on the top and one skin depth on the bottom), but of course capped by the actual thickness of the metal, i.e.,

$$d = \begin{cases} 2\delta & \text{if } t_A > 2\delta \\ t_A & \text{if } t_A \leq 2\delta. \end{cases} \quad (1)$$

The current flow through each of these distributed elements generates heat according to the distribution of current. This current

and thus the heat flux are zero at two of the antenna edges (adjacent and opposite the feed). Thus there is a high thermal conductivity path through the metal to an effective heat sink in the low current regions of the antenna. This concept was developed and verified in [12]. The heat flows through the metallization due to the difference in thermal conductivity between the heat conduction path through the metallization and the electrical substrate.

Derivation of the temperature distribution on the patch follows that used by the authors for transmission lines [12] with the difference being that on a transmission line, there is a traveling wave, and on the resonant antenna, there is a standing wave. The 1-D homogenous equation for the heat flux, $q(x,t)$ is [12]

$$\frac{\partial^2 q(x,t)}{\partial x^2} - \frac{\rho_d c_v}{k}\frac{\partial q(x,t)}{\partial t} = \frac{A_A}{V_A}\frac{\partial q(x,t)}{\partial x} \tag{2}$$

where c_v is the thermal capacity (units of $J \cdot K^{-1} \cdot kg^{-1}$), ρ_d is the density (units of $kg \cdot m^{-3}$), and k is the thermal conductivity (units of $K^{-1} \cdot W$). In (2), V_A is the incremental volume in which heat is generated, and A_A is the incremental area that the heat flux travels through. The flux is related to the temperature by

$$q(x,t) = -k\frac{\partial T(x,t)}{\partial x}. \tag{3}$$

The form of the heat equation here, i.e., (2), has a frequency response solution that is bounded at all frequencies.

The feed line here is a transmission line that is nearly matched. Heating, and thus the temperature distribution, is largely uniform along the line. As such, heat flux will be dominated by heat flow from the transmission line into the substrate. The heat generating volume will be that of the feed line, $V_F = L_F W_F d$, and the heat flux will pass through an area, $A_F = L_F W_F$. Thus $V_F/A_F = d$. The calculation of the PIM generated on the feed line is described in [12].

However on the patch, the standing wave of RF current is nearly sinusoidal with a peak at $x = 0$ and is zero at $x = \pm(1/2)L_A$. Heat flux will be in the x direction from the hot region in the center of the strip (at $x = 0$) towards the cooler regions near the edges at $x = \pm(1/2)L_A$. Since heat flux is not uniform across the antenna, it is necessary to consider an incremental heat producing volume with, referring to Fig. 2, $\Delta V_A = \Delta x \Delta y d$, and the incremental area through which flux flows is $\Delta A_A = \Delta y d$. Since the standing wave is approximately constant with respect to the y direction, these incremental quantities can be replaced by $\Delta V_A = \Delta x W d$ and $\Delta A_A = W d$, and so

$$\frac{\Delta V_A}{\Delta A_A} = \frac{V_A}{A_A} = \Delta x. \tag{4}$$

Solution of (2) is needed to determine both the constant and time-varying flux. The constant flux case defines the quiescent point of the electrical and thermal conductivity, while the periodic flux case determines the nonlinear behavior of the electro-thermal system. The boundary conditions of the constant flux system over the domain $-(1/2)L_A < x < (1/2)L_A$ are

$$q(0,t) = q_a \quad t > 0 \tag{5}$$
$$q(x,t) = 0 \quad t = 0 \tag{6}$$
$$T(x,t) = T_a \quad t = 0 \tag{7}$$

where q_a is the average heat produced in the material and T_a is the ambient temperature in the material. The temperature is, from the definition of heat flux

$$T(x,t) = \frac{1}{k}\int q(x,t)dx = \frac{q_a}{k} + T_a. \tag{8}$$

This represents the temperature rise due to the average electrical power dissipation superimposed on the ambient temperature of the material. Solution for the time-varying temperature describes the time-dependent thermal modulation of electrical conductivity. The boundary conditions for this 1-D system over the domain $-(1/2)L_A < x < (1/2)L_A$ are

$$q(0,t) = q_p \cos(\omega t - \phi) \quad t > 0 \tag{9}$$
$$q(x,t) = 0 \quad t = 0 \tag{10}$$

where q_p and ϕ are the magnitude and phase, respectively, of the periodic heat generated at radian frequency ω. The dominant components of the spectrum of the thermal system corresponds to the baseband (i.e., the envelope) of the electrical signal. For a two-tone electrical system with applied electrical tones at f_1 and f_2 with $f_1 \approx f_2$, the dominant components of the thermal system will be at DC and at the difference frequency $|f_2 - f_1|$. Thus the thermal skin depth is much larger than the electrical skin depth.

A periodic heat flux yields a solution that is periodic in time and attenuated as it propagates in space and has the form

$$q(x,t) = X(x)e^{\jmath(\omega t - \phi)} \tag{11}$$

where $X(x)$ is the heat profile of the material. Substituting this solution into (2) yields

$$\frac{\partial^2 X(x)}{\partial x^2} - \frac{A}{V}\frac{\partial X(x)}{\partial x} - \frac{\jmath\omega\rho c_v}{k}X(x) = 0 \tag{12}$$

an equation dependent only on space and periodic in time and has the general solution

$$X(x,t) = Be^{r_1 x} + Ce^{r_2 x} \tag{13}$$

with roots

$$r_1 = \frac{1 + \sqrt{1 + 4\jmath\omega\rho c_v k^{-1} V^2 A^{-2}}}{2V_A A_A^{-1}} \tag{14}$$

$$r_2 = \frac{1 - \sqrt{1 + 4\jmath\omega\rho c_v k^{-1} V^2 A^{-2}}}{2V_A A_A^{-1}}. \tag{15}$$

The term which is finite as $x \to -\infty$ and $\omega > 0$ is

$$X(x) = Be^{x r_1}. \tag{16}$$

The solution which has the value of the source at $x = 0$ is

$$q(x,t) = q_p e^{\Re(r_1)x} \cos(\omega t + \Im(r_1)x - \phi). \tag{17}$$

Now the temperature distribution is obtained as the integration of the heat flux over space:

$$T(x,t) = \frac{1}{k}\int_{-L_A/2}^{\frac{L_A}{2}} q(x,t)dx$$

$$= \frac{1}{k} \int\limits_{-L_A/2}^{\frac{L_A}{2}} q_p e^{\Re(r_1)x} \cos\left(\omega t + \Im(r_1)x - \phi\right) dx. \tag{18}$$

Integration by parts and application of the original boundary conditions yields the solution for the temperature in the conductor:

$$T(x,t) = \frac{2V_A A_A^{-1} k^{-1} q_p e^{\Re(r_1)x} \cos\left(\omega t + \Im(r_1)x - \phi\right)}{1 + \sqrt{1 + 4\jmath\omega\rho c_v k^{-1} V_A^2 A_A^{-2}}}. \tag{19}$$

B. Electro-Thermal PIM of a Finite Element on the Patch

The origin of electro-thermal PIM is the thermo-resistance effect in which the electrical resistivity, ρ_e (units of $\Omega \cdot m$), of a material is a function of temperature T [18]:

$$\rho_e(T) = \rho_{e0}(1 + \alpha T + \beta T^2 + \ldots). \tag{20}$$

Here ρ_{e0} is the static resistivity constant and α and β are constants representing the temperature coefficients of resistance (TCR). The temperature in (20) is determined by the heat in the conductor, which is a function of the electrical power. The heat generated in the volume of the incremental lossy element, ΔQ (units of $W \cdot m^{-3}$) is equivalent to the element's power dissipation

$$\Delta Q = J^2 \rho_e(T) \tag{21}$$

where J is the current density vector in unit of $A \cdot m^{-2}$. The electric field in the conductor due to the current density J is

$$E = J\rho_{e0}(f)\left[1 + \alpha(T_a + T_p)\right]. \tag{22}$$

Here T_a is the ambient temperature and T_p is the periodic temperature due to sinusoidal heating. Further terms in the series have been dropped due to the magnitude difference between α and β ($\alpha \gg \beta$) in most metals.

The nonlinear electric field in (22) is determined by the current density. For a two-tone standing wave, the current density is

$$J = J_1(x)\cos(\omega_1 t + \phi_1) + J_2(x)\cos(\omega_2 t + \phi_2). \tag{23}$$

$J_1(x)$ and $J_2(x)$ are the magnitude of the current density at x for each of the two tones with radian frequencies ω_1 and ω_2 and phases ϕ_1 and ϕ_2, respectively.

The periodic temperature, T_p, is given by (19) with q_p defined by the expansion of the dissipated power

$$\begin{aligned}
\Delta Q = {} & \frac{1}{2}\rho_e(f)\left[J_1^2(x) + J_2^2(x)\right] \\
& + \ldots \frac{1}{2}\rho_e(f)J_1^2(x)\cos(2\omega_1 t + 2\phi_1) \\
& + \ldots \frac{1}{2}\rho_e(f)J_2^2(x)\cos(2\omega_2 t + 2\phi_2) \\
& + \ldots \rho_e(f)J_1(x)J_2(x)\cos\left[(\omega_2 - \omega_1)t + (\phi_2 - \phi_1)\right] \\
& + \ldots \rho_e(f)J_1(x)J_2(x)\cos\left[(\omega_2 + \omega_1)t + (\phi_2 + \phi_1)\right]
\end{aligned} \tag{24}$$

which has a lowpass filter form and in a two-tone test only the DC and $\omega_2 - \omega_1$ component are of significance. Thus

$$\begin{aligned}
\Delta Q \approx {} & \frac{1}{2}\rho_e(f)\left[J_1^2(x) + J_2^2(x)\right] + \ldots \\
& \rho_e(f)J_1(x)J_2(x)\cos\left[(\omega_2 - \omega_1)t + (\phi_2 - \phi_1)\right]
\end{aligned} \tag{25}$$

which contains the average and periodic heat dissipated in the heat generation layer of thickness d. Thus, using (25) and replacing q by Q in (18) and considering Q to be uniform over d, the periodic temperature is

$$\begin{aligned}
& T_p(0,t) \\
& = \frac{\left[2\rho_e(1+\alpha T_a)J_1(x)J_2(x) \times k^{-1}V_A A_A^{-1} d \cos(\omega_d t - \phi_d)\right]}{1 + \sqrt{1 + 4\jmath\omega_d\rho c_v k^{-1} V_A^2 A_A^{-2}}}
\end{aligned} \tag{26}$$

where $\omega_d = \omega_2 - \omega_1$ and $\phi_d = \phi_2 - \phi_1$. The third-order PIM is then determined by expanding (22). The electric fields of the upper and lower intermodulation products (intermods) generated by each finite element are

$$E_{\omega_3}(x,t) = E_{\mathrm{PIM},U}(x)\cos\left[(2\omega_1 - \omega_2)t - (2\phi_1 - \phi_2)\right] \tag{27}$$

$$E_{\omega_4}(x,t) = E_{\mathrm{PIM},L}(x)\cos\left[(2\omega_2 - \omega_1)t - (2\phi_2 - \phi_1)\right] \tag{28}$$

where

$$E_{\mathrm{PIM},U}(x) = \chi J_1(x)J_2^2(x) \tag{29}$$

$$E_{\mathrm{PIM},L}(x) = \chi J_1^2(x)J_2(x) \tag{30}$$

$$\chi = \frac{2V_A A_A^{-1}\rho_e^2(1+\alpha d)\alpha d k^{-1}}{1 + \sqrt{1 + 4\jmath\omega_d\rho c_v k^{-1} V_A^2 A_A^{-2}}} \tag{31}$$

$\omega_3 = 2\omega_1 - \omega_2$, and $\omega_4 = 2\omega_2 - \omega_1$.

IV. ANTENNA DESIGN

The silver-on-sapphire rectangular patch antenna with an inset feed line was designed using the procedure described in [19] (see Fig. 2). The inset design matches the antenna to a 50 Ω system requiring neither a matching network nor a soldered feed point. The sapphire substrate is anisotropic with relative permittivity $\epsilon_r = 11.58$ perpendicular to the surface and $\epsilon_r = 9.3$ parallel to it. The simulated and measured return losses of the antenna are shown in Fig. 3 where the simulated and measured resonant frequencies differ by less than 0.1%.

The surface current density distribution on the antenna current is shown in Fig. 4(a) with density along vertical and horizontal cuts shown in Fig. 4(b). The simulated surface current density, J_S, on the antenna for an applied signal of 0 dBm is shown in Fig. 4. In the horizontal direction, the current has a half-sinusoidal distribution, curve (ii) in Fig. 4(b), and in the vertical direction the current distribution is nearly constant with a peaking at the edges of the antenna, curve (i) in Fig. 4(b). The minimum surface current on the vertical slice is 12.73 A/m, and this is the peak of the sinusoidal current variation in line with the feed line. Along the vertical line, curve (i), the average (along the y direction) sinusoidal peak of $J_{s,A}(0 \text{ dBm})$ is 13.21 A/m and the weighted average, weighted by the cubic power of $J_{s,A}$, is (surprisingly) 13.22 A/m. Scaling this to an input signal of
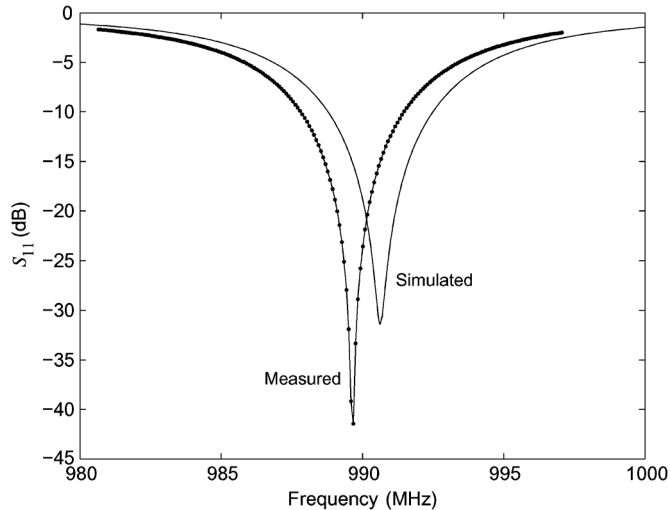
Fig. 3. S_{11} of rectangular patch antenna antenna with simulated return loss (RL) of 31.4 dB at 990.6 MHz, and measured RL of 41.4 dB at 989.7 MHz. Simulations were performed using Sonnet v12.56.

32.3 dBm, $J_{s,A}(32.3\text{ dBm})$ is 544.4 A/m and the peak current density on the patch is $J = 302.4\text{ MA/m}^2$.

V. FABRICATION

The antenna fabrication process was developed to eliminate any postulated source of antenna PIM other than the electro-thermal source. Ferromagnetic materials were eliminated in antenna fabrication, connectorization, and test equipment. The single crystal sapphire substrate has a loss tangent of 0.00002 minimizing dielectric loss and substrate discontinuities as sources of PIM. Both sides of the 100-mm diameter substrate were epi-polished to <5 A surface roughness. Together with metallization annealing, this effectively eliminated PIM attributed to surface roughness-related tunneling. The single metal design eliminates nonlinear metal junction effects that could cause PIM.

The sapphire wafer was washed with acetone and methanol to remove any film, then dried for 5 min at 500 °C. Silver was then directly sputtered onto the substrate, 1.8 μm thick with a maximum 0.2 μm variation from wafer center to wafer edge. Adhesion was achieved by annealing the sample in air for 30 min at 500 °C. Usually a seed layer such as chromium having excellent adhesion is used, but this would have formed both a dissimilar metal-metal junction when the top conductor was deposited, and could result in undesirable effects. The skin depth, δ, at 985 MHz is 2.03 μm for single crystal silver which is increased for fabricated metals [20, Appendix D]. Even in the ideal single crystal case, the antenna thickness $t_A = 1.8$ μm is less than δ.

Photo-resist was applied, UV patterned, and etched with CR-7 etchant. The photoresist was then removed and the wafer cleaned with acetone, methanol, and deionized water rinses. The wafer was then sputtered on the back side and annealed at 500 °C for 30 min, providing a high conductivity ground plane. The device was washed again and stored in a nitrogen atmosphere to prevent oxide or sulphide formation. The roughness of the bottom of the antenna corresponded to that of the substrate.
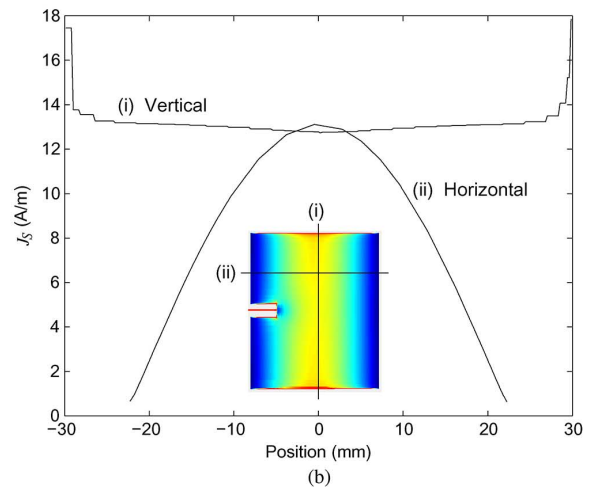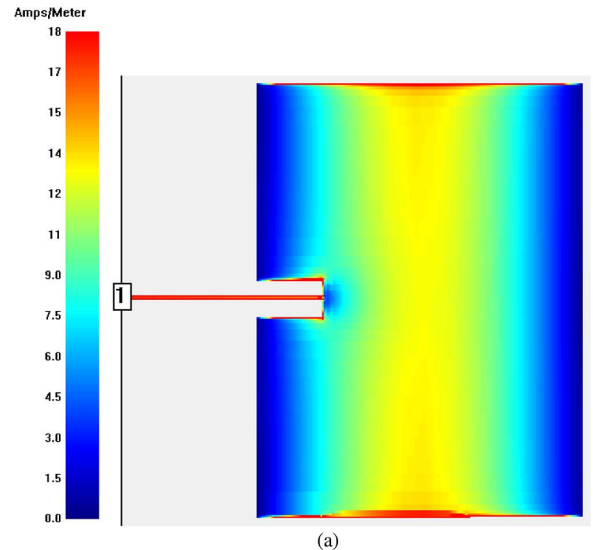

Fig. 4. Simulated surface current density, J_S, on the antenna at resonance (990.6 MHz). Simulations were performed using Sonnet v12.56 with 0-dBm input.

Surface roughness on the top metal was controlled by annealing the device to form extremely flat grains free of constriction resistances. Typical SEM images were previously presented as [12, Figs. 3 and 4] and the same process was used to produce the patch antenna. The metallization surface roughness was negligible, excellent adhesion of the substrate and metallization was achieved, and the silver metallization was extremely flat with tightly packed grains and no voids. The metal resistivity was only 7% greater than ideal single crystal resistivity.

The antenna was interfaced to the test system using the printed circuit board (PCB) assembly shown in Fig. 5. The traces on the PCB board are gold-on-copper coplanar waveguide (CPW) providing a 50 Ω transmission line from wirebonds to the antenna and external connectorization. These interfaces further reduce any current in the copper metallization. Silver conductive paint, 50% by weight, assured connection from the ground plane of the antenna to the ground plane on the top of the PCB. Gold and silver form an isomorphous alloy system due to their FCC lattice structure and comparable size resulting in no metal-oxide-metal regions at the wirebonds and a continuous metal-metal contact system [21]. Tunneling and
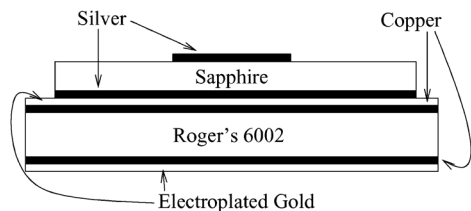
Fig. 5. Rectangular patch antenna assembly where a silver-on-sapphire antenna is mounted on a 5 μm-thick gold electroplated copper PCB board (Roger's 6002). Gold wirebonding (each being 5 parallel 1-mm-long 1-mil-diameter gold bond wires) is from the feed line on the top silver layer to the gold surface of the PCB.
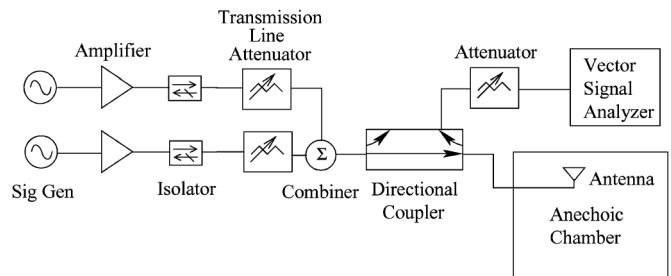

Fig. 6. Reflection configuration for antenna PIM measurement. Each channel of the system contains a signal source, amplifier, four series isolators, and a 3.5-dB transmission line attenuator. The channels are combined using a hybrid combiner with one port terminated in a low PIM cable termination and the other port connected to the DUT.

constriction resistance from wirebonding is virtually eliminated in this wirebonding arrangement.

The external connectorization used half of a custom Spinner ATL low PIM N-male to N-male helical copper encased cable, guaranteed to exhibit −160 dBc or less PIM for a two-tone input signal each being 44 dBm. The cable was cut in half and the inner and outer conductors silver soldered to the CPW PCB traces.

The complete test configuration has no ferromagnetic materials, metal-oxide-metal structures, feed point contacts, minimum dielectric loss, and minimal surface roughness.

VI. ANTENNA MEASUREMENT

Transmission PIM measurement used the two-port PIM measurement system described in [22] with the DUT replaced by the subject antenna connected to Port 1 and an identical patch antenna at Port 2. The antennas were in an anechoic chamber with low PIM helical cables connecting the antennas to the external PIM test system. The path loss was 25 dB so that the level of the two-tone signals was considerably attenuated at the second antenna and PIM from the second antenna could therefore be discounted. The system dynamic range was 100 dBc for a 10-Hz tone separation reducing to 85 dBc for a 200-kHz tone separation.

The test configuration for reflection measurement of PIM is shown in Fig. 6. This enabled much lower levels of PIM to be measured than could be measured in the transmission configuration since the two applied tones were effectively attenuated by the return loss of the antenna. The PIM energy generated on the antenna is equally radiated and reflected, and the return loss of the antenna, which affects only the test signal, effectively enhances dynamic range. The test set used silver-plated connectors, well heat-sinked components, and low PIM cables. Also low PIM transmission line 3.5-dB attenuators (50 Ω microstrip PCB lines) and low PIM cable terminations were used. Each decibel of attenuation enhanced the dynamic range of the test system by 2 dB due to the decreased signal power in the isolators. However there is a limit to what can be gained, with the 3.5 dB of attenuation prior to the combiner found to be optimum. With a 22-dB attenuator between the directional coupler and the vector signal analyzer and the return loss of the antenna increased to 50 dB by placing an absorber tile over the antenna, the dynamic range of the system was determined to be 125 dB for a 1-Hz tone separation. This reduces to 103 dB for a 100-kHz tone separation because of the reduced return loss away from the center frequency of the antenna.

VII. RESULTS AND DISCUSSION

The electro-thermal PIM model of the rectangular patch antenna on sapphire can be determined from material parameters alone. In the analysis of transmission lines in [12], all of the heat traveled into the substrate due to the almost even heating of the metal. This describes the situation with the feed line portion of the microstrip antenna here. However with the patch portion of the antenna, the standing wave results in unevenly heated metal regions. The thermal conductance through the metal between unevenly heated regions is over two orders of magnitude higher than that of the substrate. Thus the thermal properties of the metal dominates PIM on the resonant antenna (and of all structures with standing waves), whereas the thermal properties of the substrate dominates PIM generation of transmission lines with low VSWR. Table I details the thermal and electrical parameters necessary to model PIM. The measured DC resistivity of the fabricated silver was 17.0 ± 0.5 n$\Omega \cdot$ m, which is only 7% more than the resistivity of single crystal silver, which is 15.87 n$\Omega \cdot$ m. The power of each tone of the two-tone signal was 32.3 dBm. The PIM generated on the feed line was calculated using the procedure described in [12] and that on the patch using (29) and the procedure described in the Appendix. In this method, the PIM at the two ends of the transmission line are separately calculated, and only the backward-traveling PIM wave at the antenna port was considered as the other end of the feed line and is matched to the antenna and radiated. Half of the patch-generated PIM is radiated and half presented to the feed line, and since the patch is matched to the feed line, this PIM appeared at the measurement port. The simulated PIM at the measurement port due to the antenna and due to the feed line are shown in Fig. 7 as curves (iii) and (i), respectively. The combined PIM not calculated as the phasing of the two PIM sources was not apparent from the analysis.

Fig. 7 presents measurements of the reflected PIM for 3-Hz to 100-kHz tone separation at a center frequency of 989 MHz. Below 8-Hz tone separation, the measured reflected PIM is apparently due to the higher PIM (as calculated) of the patch. Above 20-Hz the measurements match the PIM calculated for the feed line. The measurements were performed quickly enough that static heating of the antenna was not significant as this was found to shift the center frequency of the antenna otherwise. Transmission measurements are also shown in Fig. 7. The dynamic range of the transmission test system was much less than that of the reflection system and only two measurements are shown (at 3 Hz and 10 Hz). Even with
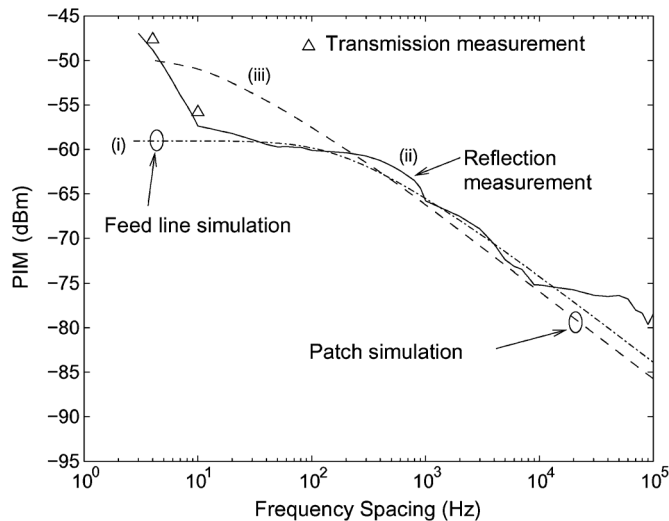
Fig. 7. Silver-on-sapphire rectangular patch antenna is two-tone tested in both a transmission and reflection configuration at 32.3-dBm input power. The frequency separation is swept from 3 Hz to 100 kHz for the reflection measurement and is conducted at 4 Hz and 10 Hz tone separation for the transmission measurement. Both measurements are compared against electro-thermal model simulation results for both the antenna element and the feed line.

TABLE I
SILVER-ON-SAPPHIRE ANTENNA SIMULATION PARAMETERS (AT 300 K)

Structure	Thermal conductivity, k ($\mathrm{W \cdot m^{-1} K^{-1}}$)	Thermal capacity, c_v ($\mathrm{J \cdot kg^{-1} K^{-1}}$)	Density, ρ_D ($\mathrm{kg \cdot m^{-3}}$)	Electrical resistivity, ρ_e ($\mathrm{n\Omega \cdot m}$)
Silver	429	232	10490	17.0
Sapphire	25	740	3980	

the limited transmission measurements, the premise of equal reflected and radiated PIM is supported. Thus to characterize the PIM produced by an antenna when operated in band, it is only necessary to measure the reflected PIM. This conjecture would apply to any other source of PIM as a PIM source is a point source that will propagate equally in all directions in a matched system.

The calculated PIM of the feed line has a corner frequency of approximately 300 Hz and above that has a 10-dB decrease of PIM per decade of tone separation. For the patch, the corner frequency is 20 Hz and above that, a 10-dB decrease of PIM per decade of tone separation is observed again. These are the classic signatures of electro-thermal-sourced PIM [12], [17]. The measured PIM matches the combination of the modeled feed line and patch PIM taking into account the uncertain vector addition of the two sources of PIM in the 10–100 Hz range.

VIII. DESIGN GUIDELINES

Electro-thermally induced PIM is due to the variation of conductance as temperature varies in response to the time-varying power dissipated by RF signals with nonconstant envelopes. PIM is a source of co-site interference when large high power transmitters are mounted near sensitive receivers. With communication systems, it is the widely-separated tone case that is most problematic, and in relation to the results presented here, this means that high tone-separations are of most concern. PIM in this case is reduced by providing immediate heatsinking

using metals that have high conductivity and are thick, even much thicker than the electrical skin depth. Relative to most substrates, only metal has sufficient thermal conductivity to heatsink the electro-thermal effect that results from envelopes varying at hundreds of Hz or higher. Alternative designs, e.g., a patch antenna on a thick substrate, can have larger dimensions and reduced current densities. Using substrates with very high thermal conductivities will also reduce PIM. The power dissipated in antennas is almost entirely due to resistive losses so the primary strategy to reducing PIM in antennas is to minimize losses, minimize current density, and provide good heatsinking. Losses can be minimized by using thick metalization and avoiding constriction resistances which, for example, are significant in mesh antennas commonly used in space-borne and portable antennas.

IX. CONCLUSION

In this paper, electro-thermal conductivity modulation was introduced as a mechanism producing passive intermodulation (PIM) in resonant antenna structures. Thermal effects have often been overlooked as the relaxation times between thermal and electrical systems are considered to be offset by several orders of magnitude. However envelope modulation produces power components of the electrical signal within thermal relaxation times and results in PIM generation due to electro-thermal coupling. A theoretical analysis of heat conduction and electro-thermal interaction was presented resulting in an expression for electro-thermal PIM based on time-varying current density distribution. The model closely matched reflection and transmission measurements of PIM. It was shown that, in-band, the reflected and transmitted PIM generated on an antenna are equal and it is sufficient (and easier) to measure reflected PIM to characterize the PIM performance of an antenna.

The antenna fabricated here was constructed to minimize proposed sources of PIM other than PIM resulting from an electro-thermal effect. Principally this was achieved by eliminating roughness and leaving out an adhesion layer between the high-conductivity metal and the substrate. It is believed that other sources of PIM for antennas can be important. Though there are a large number of theories, the precise physical mechanism for these other sources of PIM has not been identified experimentally.

APPENDIX

This appendix documents the procedure for calculating upper sideband PIM on the antenna. The circuit model is shown in Fig. 8. The PIM presented at the antenna port comprises the upper-sideband PIM power derived from the patch, $P'_{A,\mathrm{PIM},U}$, and PIM due to the feed line $P_{F,\mathrm{PIM},U}$. For the patch, the PIM generating mechanism is modeled as a series of voltage generators with voltage $\Delta V_{\mathrm{PIM},U}$ so that the total PIM voltage is $V_{\mathrm{PIM},U} = \sum \Delta V_{\mathrm{PIM},U}$. Each of these voltages generators contributes a PIM current $\Delta I_{\mathrm{PIM},U}$ to the PIM standing wave so that the total PIM current is $I_{\mathrm{PIM},U} = \sum \Delta I_{\mathrm{PIM},U}$.

The PIM power of the upper IM3 tone at ω_3 produced by the incremental volume of length $\Delta x = 1$ mm was calculated from $E_{\mathrm{PIM},U}(x)$ using (29) and the assumption of a standing current wave on the antenna at resonance (with $f_1 \approx f_2$):

$$J_1(x) = J_2(x) = \frac{J_{s,A}}{d} \cos\left(\frac{\pi x}{L_A}\right). \tag{32}$$
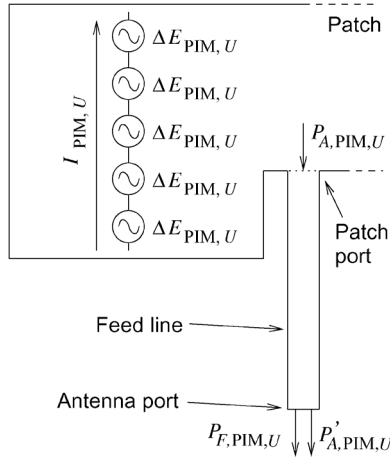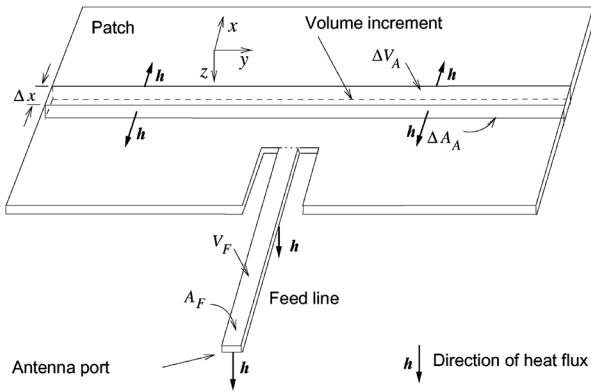
Fig. 8. Model used in calculating PIM.

Fig. 9. Microstrip antenna showing the volume increment on the patch.

Here $J_{s,A}$ is the peak surface current density (at $x = 0$) on the patch and is a function of the input power of one tone, and d is the thickness of the current carrying region on the patch; see (1). $J_{s,A}$ at 0-dBm available input power of one tone was calculated using EM simulation (as for Figs. 3 and 4), yielding $J_{s,A}(0 \text{ dBm}) = 13.2 \text{ A/m}$. The current density was scaled for other power levels.

For the patch, heating is uniform in the y and z directions but not in the x direction as there is a standing wave of current. Thus the largest incremental volume producing heat on the patch is shown in Fig. 9 and has width W_A, thickness d, and length Δx. The volume of this element is $V_A = \Delta x W_A t_A$. Since the heat produced on the antenna is concentrated in the center (with respect to x) of the patch, heat flows from hot regions to cooler regions in the plane of the antenna. In particular, for an element at x, heat flows in the $-x$ direction if $x < 0$ and in the $+x$ direction if $x > 0$. Thus the heat flux passes through a cross-section of area $A_A = W_A t_A$, so that the geometric parameter for the antenna patch is $V/A = (V_A/A_A) = \Delta x$. Here $\Delta x = 1$ mm and the calculation is relatively independent of this choice provided it is not too large. Heat flux into the substrate is not explicitly considered as the thermal conductivity of the silver conductor, $429 \text{W} \cdot \text{m}^{-1} \cdot \text{K}^{-1}$, is much higher than that of the sapphire substrate, $25 \text{W} \cdot \text{m}^{-1} \cdot \text{K}^{-1}$. Implicitly, heat flux into the substrate creates the cooler regions which act as a heat sink. This simplifying assumption avoids the complexity of developing a quasi-analytic solution of the heat flux in the x–z plane simultaneously in both the metal and the substrate.

The current contributed by each PIM generator is

$$\Delta I_{\text{PIM},U} = \rho_e^{-1} W_A d \Delta x^{-1} \Delta V_{\text{PIM},U} = \rho_e^{-1} W_A d \Delta E_{\text{PIM},U}. \tag{33}$$

As the patch is resonant and there is a current standing wave, these current contributions integrate (they are summed) here to produce the total PIM current and voltage:

$$I_{\text{PIM},U} = \sum_{\Delta x} \Delta I_{\text{PIM},U}, \quad V_{\text{PIM},U} = \sum_{\Delta x} \Delta V_{\text{PIM},U}. \tag{34}$$

Then the total power of the PIM generated on the patch is

$$P_{\text{PIM},U}^T = \frac{1}{2} I_{\text{PIM},U} V_{\text{PIM},U} \tag{35}$$

where the $1/2$ is because the voltage and currents are amplitudes of periodic time-varying quantities. For example, with the available power of each tone being 32.3 dBm and the tones centered at 990.6 MHz and offset by 100 kHz, the total upper-sideband PIM power produced on the patch is $P_{A,\text{PIM},U}^T = -82.8$ dBm.

At resonance, the microstrip patch antenna is matched to both free space and the feed line so that the single-tone PIM power, $P_{A,\text{PIM}}$, presented to the input of the feed line is 3 dB lower than $P_{A,\text{PIM},U}^T$ and is further reduced by the calculated 0.05-dB loss of the feed line. Thus at the input of the feed line, the PIM produced by the patch is $P_{A,\text{PIM},U}' = -85.9$ dBm. The radiated upper-sideband PIM power is 3 dB less than $P_{A,\text{PIM},U}^T$. The $P_{A,\text{PIM}}$ calculated is sensitive to the current density which is derived from the simulated surface current density $J_{s,A}(0 \text{ dBm})$. For example, if the actual current density is 12% lower, then the $P_{A,\text{PIM}}$ calculated will be 3 dB lower.

Calculation of the PIM produced on the feed line follows the procedure presented in [12]. The transmission line has uniform heating along its length as VSWR ≈ 1. As such, the maximum uniform heat producing volume of the feed line is $V_F = L_F W_F d$. Heat flux now is directed into the sapphire substrate so that the area the flux passes through is $A_F = L_F W_F$ and so the geometric parameter $V/A = (V_F/A_F) = d$. PIM presented at the ports of the transmission line are the integrals of traveling PIM waves produced along the feed line. The backward traveling component of feed line PIM is presented at the input port of the antenna structure, and the forward-traveling PIM is radiated by the patch antenna.

References

[1] Y. Patenaude, J. Dallaire, F. Menard, and S. Richard, "Antenna PIM measurements and associated test facilities," in *Proc. IEEE Antennas and Propagation Society Int. Symp.*, Jul. 2001, vol. 4, pp. 620–623.

[2] V. Golikov, S. Hienonen, and P. Vainikainen, "Passive intermodulation distortion measurements in mobile communication antennas," in *Proc. Veh. Technol. Conf.*, Oct. 2001, pp. 2623–2625.

[3] P. L. Lui and A. D. Rawlins, "Passive non-linearities in antenna systems," in *Proc. IEEE Colloq. Passive Intermodulation Products in Antennas and Related Structures*, Jun. 1989, pp. 6/1–6/7.

[4] V. Lubrano, R. Mizzoni, F. Silvestrucci, D. Raboso, and A. Spazio, "PIM characterisitcs of the large deployable reflector antenna mesh," in *Proc. 4th Int. Workshop Multipactor, Corona and Passive Intermodulation in Space RF Hardware*, Sep. 2003.

[5] V. Golikov, S. Hienonen, and P. Vainikainen, "Passive intermodulation distortion measurements in mobile communication antennas," in *Proc. 54th Veh. Technol. Conf.*, Oct. 2001, pp. 2623–2625.

[6] P. Bolli, S. Selleri, and G. Pelosi, "Passive intermodulation on large reflector antennas," *IEEE Antennas Propag. Mag.*, vol. 44, no. 5, pp. 13–20, Oct. 2002.

[7] W. H. Higa, "Spurious signals generated by electron tunneling on large reflector antennas," *Proc. IEEE*, vol. 63, no. 2, pp. 306–313, Feb. 1975.

[8] J. G. Simmons, "Generalized formula for the electric tunnel effect between similar electrodes separated by a thin insulating film," *Appl. Phys.*, vol. 34, no. 6, pp. 1793–1803, Jun. 1963.

[9] S. Hienonen, V. Golikov, P. Vainikainen, and A. Raisanen, "Near-field scanner for the detection of passive intermodulation sources in base station antennas," *IEEE Trans. Electromagn. Compatibil.*, vol. 46, no. 4, pp. 661–667, Nov. 2004.

[10] J. Sanford, "Passive intermodulation considerations in antenna design," in *Proc. Antennas and Propagation Society Int. Symp.*, Jun. 1993, pp. 1651–1654.

[11] J. R. Wilkerson, K. G. Gard, and M. B. Steer, "Electro-thermal passive intermodulation distortion in microwave attenuators," in *Proc. 36th Eur. Microwave Conf.*, Sep. 2006, pp. 157–160.

[12] J. R. Wilkerson, K. G. Gard, and M. B. Steer, "Distributed passive intermodulation distortion on transmission lines," *IEEE Trans. Microwave Theory Techn.*, vol. 59, no. 5, pp. 1190–1205, May 2011.

[13] S. Melamed, T. Thorolfsson, T. R. Harris, S. Priyadarshi, P. Franzon, M. B. Steer, and W. R. Davis, "Junction-level thermal analysis of 3-d integrated circuits using high definition power blurring," *IEEE Trans. Comput.-Aided Design Integr. Circuits Systems*, vol. 31, no. 5, pp. 676–689, 2012.

[14] T. R. Harris, S. Priyadarshi, S. Melamed, C. Ortega, R. Manohar, S. R. Dooley, N. M. Kriplani, W. R. Davis, P. D. Franzon, and M. B. Steer, "A transient electrothermal analysis of three-dimensional integrated circuits," *IEEE Trans. Compon., Packag., Manuf. Technol.*, vol. 2, no. 4, pp. 660–667, 2012.

[15] S. Luniya, W. Batty, V. Caccamesi, M. Garcia, C. Christoffersen, S. Melamed, W. R. Davis, and M. Steer, "Compact electrothermal modeling of an x-band mmic," in *Proc. 2006 IEEE MTT-S Int. Microwave Symp. Digest*, 2006, pp. 651–654.

[16] W. Batty, C. E. Christoffersen, A. B. Yakovlev, J. F. Whitaker, A. Mortazawi, A. Al-Zayed, M. Ozkar, S. C. Ortiz, R. M. Reano, and K. Yang *et al.*, "Global coupled em-electrical-thermal simulation and experimental validation for a spatial power combining mmic array," *IEEE Trans. Microwave Theory Techn.*, vol. 50, no. 12, pp. 2820–2833, Dec. 2002.

[17] J. R. Wilkerson, K. G. Gard, A. G. Schuchinsky, and M. B. Steer, "Electro-thermal theory of intermodulation distortion in lossy microwave components," *IEEE Trans. Microwave Theory Techn.*, vol. 56, no. 12, pp. 2717–2725, Dec. 2008.

[18] T. Bechtold, E. B. Rudnyi, and J. G. Korvink, "Dynamic electrothermal simulation of Microsystems a review," *J. Micromech. Microeng.*, vol. 15, no. 11, p. R17, 2005.

[19] C. Balanis, *Antenna Theory Analysis and Design*, 3rd ed.   Hoboken, NJ, USA: Wiley, 2005.

[20] M. Steer, *Microwave and RF Design: A Systems Approach*, 2nd ed.   Raleigh, NC, USA: SciTech, 2013.

[21] C. Chuang and J. Aoh, "Thermosonic bonding of gold wire onto silver bonding layer on the bond pads of chips with copper interconnects," *Electron. Mater.*, vol. 35, no. 9, pp. 1693–1700, Sep. 2006.

[22] J. R. Wilkerson, P. G. Lam, K. G. Gard, and M. B. Steer, "Automated broadband high-dynamic-range nonlinear distortion measurement system," *IEEE Trans. Microwave Theory Techn.*, vol. 58, no. 5, pp. 1273–1282, May 2010.

Ian M. Kilgore (S'10) received the B.S. degree in electrical engineering from North Carolina State University (NCSU), Raleigh, NC, USA, in 2013 and is currently pursuing the Ph.D. degree at NCSU.

He is a Graduate Research Assistant at NCSU.

Kevin G. Gard (M'91) received the B.S. and M.S. degrees in electrical engineering from North Carolina State University (NCSU), Raleigh, NC, USA, in 1994 and 1995, respectively, and the Ph.D. degree in electrical engineering from the University of California at San Diego, La Jolla, CA, USA, in 2003.

In 2010, he joined Analog Devices Inc., Raleigh, NC, USA, as a radio frequency integrated circuit (RFIC) design and system engineer developing wireless receiver systems in 65-nm CMOS. During 2009, he was an RFIC development engineer ST Ericsson where he designed a multi-band low-noise amplifier front-end circuit in 90-nm CMOS for GSM, EDGE, and WCDMA transceivers. From 2004 to 2008, he was the William J. Pratt Assistant Professor with the Electrical and Computer Engineering Department at NCSU. From 1996 to 2003, he was with Qualcomm Inc., San Diego, CA, USA, where he was a Staff Engineer and Manager responsible for the design and development of RFICs for code-division multiple-access (CDMA) wireless products. Since 2009, he has been an adjunct assistant professor in the Electrical and Computer Engineering Department of NCSU. His research interests are in the areas of novel integrated circuit solutions for wireless transceivers and analysis of nonlinear microwave circuits with digitally modulated signals. He has authored or coauthored over 70 papers related to RF/analog integrated circuit design and analysis of nonlinear circuits.

Dr. Gard is a member of the IEEE Microwave Theory and Techniques Society (IEEE MTT-S) and IEEE Solid-State Circuits Society. In 2007, he was secretary of the IEEE MTT-S Administrative Committee (AdCom). In 2010, he was co-recipient of the Microwave Prize from the IEEE Microwave Theory and Techniques Society. In 2007, he was a co-recipient of a NASA Group Achievement Award.

Jonathan R. Wilkerson (S'08–M'10) received B.S. degrees in electrical engineering and computer engineering in 2005, the M.S. degree in electrical engineering in 2006, and the Ph.D. degree in electrical engineering in 2010 from North Carolina State University, Raleigh, NC, USA.

In 2014, he joined Eyenovia as the engineering director developing high-volume manufacturing processes for piezoelectric based micro-fluidic drug delivery systems. From 2011–2013, he was the engineering director at Corinthian Ophthalmic where he developed piezoelectric-based micro-fluidic drug delivery systems. He started his career at Physical Devices in 2010 as a co-founder, where he worked on antijamming and tunable filters for military applications. His current research interests include electrothermal systems, thermo-acoustic systems, man-machine interfaces, and RF-inspired cryptography. He has one issued patent, nine pending patents, and has authored or coauthored 14 papers related to RF/analog integrated circuit design and analysis of nonlinear circuits.

Dr. Wilkerson is a member of the IEEE Microwave Theory and Techniques Society (IEEE MTT-S), the IEEE Antennas and Propagation Society, and the IEEE Signal Processing Society. In 2010, he was co-recipient of the Microwave Prize from the IEEE Microwave Theory and Techniques Society.

Michael B. Steer (S'76–M'78–SM'90–F'99) is the Lampe Distinguished Professor of Electrical and Computer Engineering at North Carolina State University (NC State), Raleigh, NC, USA. He has authored more than 470 publications and 3 books including the textbook *Microwave and RF Design: A Systems Approach*.

Prof. Steer was Secretary of the IEEE Microwave Theory and Techniques Society (MTT-S) in 1997 and was a member of the MTT-S Administrative Committee from 1998 to 2001, and from 2003 to 2006. He is a former Editor-In-Chief of the IEEE TRANSACTIONS ON MICROWAVE THEORY AND TECHNIQUES. He received the Presidential Young Investigator Award in 1986; he was the Jack S. Kilby Lecturer in 2003; and in 1994 and 1996 received the *Bronze Medallion* from U.S. Army Research for Outstanding Scientific Accomplishment. In 2007, he received a Distinguished Service Recognition Award from IEEE MTT-S. He received the 2010 Microwave Prize for the best paper on Microwave Engineering in any IEEE Publication in the preceding year. In 2011, he received the Distinguished Educator Award from IEEE/MTT-S, was inducted into the Electronic Warfare Technology Hall of Fame sponsored by the Association of Old Crows, and was named one of the Most Creative Teachers in the South by *Oxford American Magazine*. In 2013, he received the R.J. Reynolds Award for Excellence in Teaching, Research, and Extension from the College of Engineering at NC State University.